Horizon 2020
European Union funding
for Research & Innovation

E-Infrastructures

H2020-EINFRA-2015-1

EINFRA-5-2015: Centres of Excellence for computing applications

EoCoE

Energy oriented Center of Excellence for computing applications

Grant Agreement Number: EINFRA-676629

D3.3 M30

Properties and characterization of materials

Project and Deliverable Information Sheet

EoCoE	Project Ref:	EINFRA-676629
	Project Title:	Energy oriented Centre of Excellence
	Project Web Site:	http://www.eocoe.eu
	Deliverable ID:	D3.3 M30
	Lead Beneficiary:	CEA
	Contact:	Edouard Audit
	Contact's e-mail:	edouard.audit@cea.fr
	Deliverable Nature:	Report
	Dissemination Level:	PU*
	Contractual Date of Delivery:	31/03/2018
	Actual Date of Delivery:	06/04/2018
	EC Project Officer:	Carlos Morais-Pires

* - The dissemination level are indicated as follows: PU – Public, CO – Confidential, only for members of the consortium (including the Commission Services) CL – Classified, as referred to in Commission Decision 2991/844/EC.

Document Control Sheet

Document	Title :	Properties and characterization of materials
	ID :	D3.3 M30
	Available at:	http://www.eocoe.eu
	Software tool:	LaTeX
Authorship	Written by:	M. Salanne (MdlS)
	Contributors:	M. Celino (ENEA), D. Borgis (MdlS), G. Jeanmairet (MdlS), A. Walker (UBAH), U. Aeberhard (JUELICH), S. Giusepponi (ENEA), M. Gusso (ENEA)
	Reviewed by:	PEC members

Document Keywords:
Atomic-scale design, DFT, Inorganic Photovoltaic (iPV), Organic Photovoltaic (oPV), Perovskite, Supercapacitors.

Executive Summary:
Development of characterization methods and tools to address structural, electronic and optical properties of materials from the atomic-scale models. Characterization procedures to assess the reliability of the numerical models. Application of MDFT code to supercapacitor materials screening. Coupling of codes to increase accurateness of the computed properties. Modeling of materials at different lenght scales. Description of applications via continuous models. Model settings to design large scale simulations to address accurately macroscopic properties.

Contents

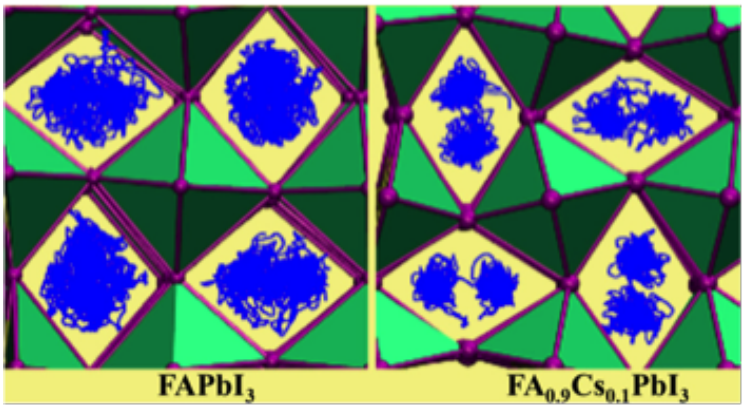

Figure 1: Dynamics of the FA^+ cation in mixed-cation perovskite phases. Density plot showing positions of nitrogen atoms of $CH(NH_2)^{2+}$ accumulated over time in $FAPbI_3$ and in $FA_{0.9}Cs_{0.1}PbI_3$. Table of contents figure of reference [1].

1. Properties and characterization of perovskite materials

1.1 Structure of the materials

Cation mixing in Lead Iodide Perovskite is being studied by Density Functional Theory (DFT) based calculations using the CP2K code. The parent tetragonal phase of $MAPbI_3$ lattice is modelled by large supercells e.g. 3x3x2 containing 48 A-site cations, which allowed us to simulate small concentrations of other cations (up to 5 %). The calculations employ an auxiliary plane wave basis set, an energy cut-off of 350 Ry, an analytical dual-space pseudopotential as implemented by Goedecker, Teter, and Hutter (GTH) and the GGA of Perdew-Burke-Ernzerhof (PBEsol). Additionally, we apply van der Waals interactions, as prescribed by Grimme. To obtain the ground state geometry, we relax all atoms till the interatomic forces become less than 0.02 eV/Å.

A brief summary of published and submitted papers and papers in preparation is given below :

1. We showed that substitution of low concentrations of smaller cations on the A-site in formamidimium lead iodide ($CH(NH_2)_2PbI_3$) results in a global ``locking'' of the PbI_6 octahedra tilting. In the locked structure the octahedra tilt at a larger angle but undergo a much reduced amplitude of rocking motion. A key impact of this feature is that the rotational or tumbling motion of the $CH(NH_2)^{2+}$ molecular ion in a locked cage is severely restricted (see 1).

2. Mixed azetidinium-methylammonium cells were shown by the experimental group headed by Cameron to give improved performance and reduced hysteresis compared to $MAPbI_3$ and these effects were explained by our model . Figure 2 shows the effects of incorporation of an Az^+ cation into the perovskite semiconductor $MAPbI_3$ where MA is methyl-ammonium. Our electronic structure calculations demonstrated that the substitution of up to 5 % Az^+ into $MAPbI_3$ is energetically favourable and that phase separation does not occur at these concentration.
   We have made calculations to support the first experimental demonstration of the family of lead-free binary metal perovskites based on tin and germanium, $CH_3NH_3Sn_XGe_{1-X}$ I_3 $(0 \leq X \leq 1)$ made by the group of Friend, University of Cambridge. Our work corroborates the structural findings of this group and ex-

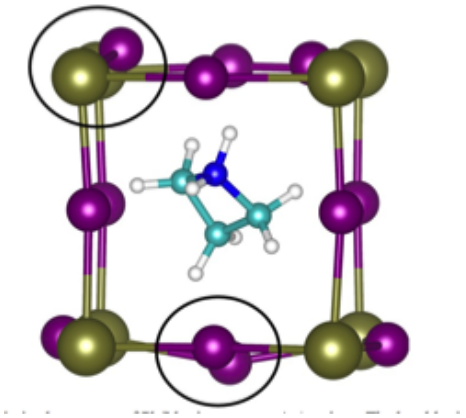

Figure 2: The optimized geometry of Pb/I lattices near to Az^+ cations. The local lattice distortion of Pb/I frame due to the presence of Az^+ cation can be seen and is emphasised by the black circles. Fig. S8 of reference [2].

plains the good thermodynamic stability of this family of perovskites.

3. A device Monte Carlo simulation code using particle-particle simulation methods for delocalized electrons in crystalline semiconductors [3] is being adapted to include ion motion. This code predicts solar cell characteristics. Its aim is to bridge the gap between the atomistic simulations described above and the continuum simulations described below. It will allow us to use information from the former to calculate scattering rates of the free charges and defect hopping rates and to understand in more detail the processes at the interfaces between perovskite and electron and hole transport layers.

1.2 Dynamics inside perovskite structures

Work is underway to boost Kinetic Monte Carlo simulations by implementing multilevel stochastic simulation techniques [4]. The multi-level method for discrete state systems, first introduced by Anderson and Higham [5], is a highly efficient simulation technique that was used in order to elucidate statistical characteristics of biochemical reaction networks[3]. A single point estimator is produced in a cost-effective manner by combining estimators of differing accuracy in a telescoping sum, and, as such, the method has the potential to revolutionise the field of stochastic simulation. Preliminary results have been obtained by applying this method to the Bath KMC code. Fast and massively parallel Poisson solvers are being developed as an additional means of speeding up the KMC. To date we have shown that the particle-mesh method [3] is an effective approach compared to summing pairwise Coulomb interactions. Further speedups in parallelisable code are anticipated.

1.3 Extension to continuum methods

A theoretical investigation of the effects of the transport layers on anomalous hysteresis in the current-voltage curves and the steady state performance of perovskite solar cells is presented. A model for ion motion and charge transport [6] has been generalised to a three-layer planar perovskite solar cell [7]. The results, illustrated in Figure 3, demonstrate that the choice of low permittivity and weakly (or un) doped transport layer

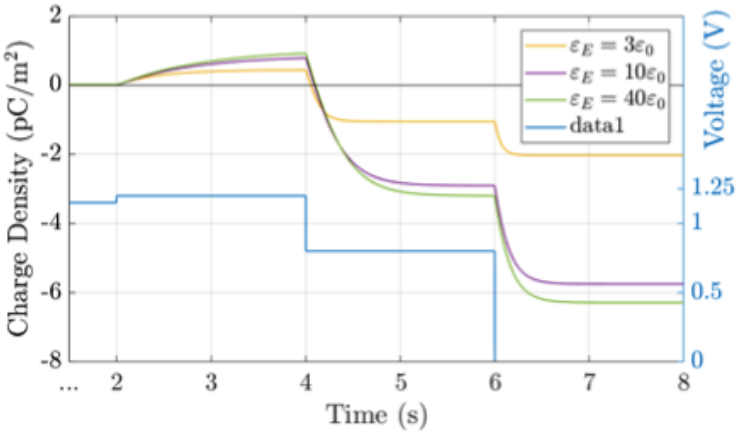

Figure 3: Evolution of the charge density due to ionic defect accumulation within 10 nm of the perovskite layer adjacent to the electron transport layer during the voltage transient (blue line). Simulations are performed for dielectric constants $\epsilon = (3; 10; 40)\epsilon_0$. Taken from reference [7].

materials leads to a shift in the scan rates at which hysteresis is observed to much higher frequencies than commonly used in experiment. This observation is consistent with published experimental results showing that current-voltage hysteresis re-emerges in so-called ``hysteresis-free'' cells at low temperature. Simulations are also used to classify features of current-voltage curves that enable the practitioner to distinguish between cells in which charge carrier recombination occurs predominantly at the interfaces between the perovskite and transport layers and those in which the recombination occurs within the perovskite. Features of the steady-state solution are used to suggest ways in which the amount of interface recombination can be reduced via the selection of transport layer properties in order to augment cell performance.

2. Characterization of the structure of a-Si:H/c-Si interfaces

The c-Si/a-Si:H interface is analysed using PWscf code of the QE suite [8, 9]. In view of the large-scale molecular dynamics simulations, a supercell approach is used to simulate the a-Si:H/c-Si interface with PBC meant to mimic an infinitely extended system. A void region of about 10 Å in z-direction is adequate to suppress the interaction between the external surfaces (this distance was checked by convergence test with respect to the void's size), then the structure is infinitely extended in both x and y directions and the interface is perpendicular to the z-direction. Further computational details are reported in Ref. [10].

As shown in Fig. 4a), the interface is built by putting nearby two free surfaces obtained cutting both the crystalline silicon and the hydrogenated amorphous silicon. The relaxed p(2×1) symmetric reconstruction of the Si(001) surface constitutes the c-Si side of the interface. It is formed by 192 Si atoms: 12 layers of silicon each of them with 16 atoms. The a-Si:H side of the system is generated using a simulate annealing quench from a melt simulation protocol. It is composed of 128 Si atoms and 16 H atoms. The total length of the system is L_z= 38.66 Å, while in the x and y direction the system has L_x= L_y= 15.46 Å. In view of long time simulations, the Brillouin zone integration is sampled at Gamma point (using the cut-off values: 40 and 240 Ry), in order to save computational

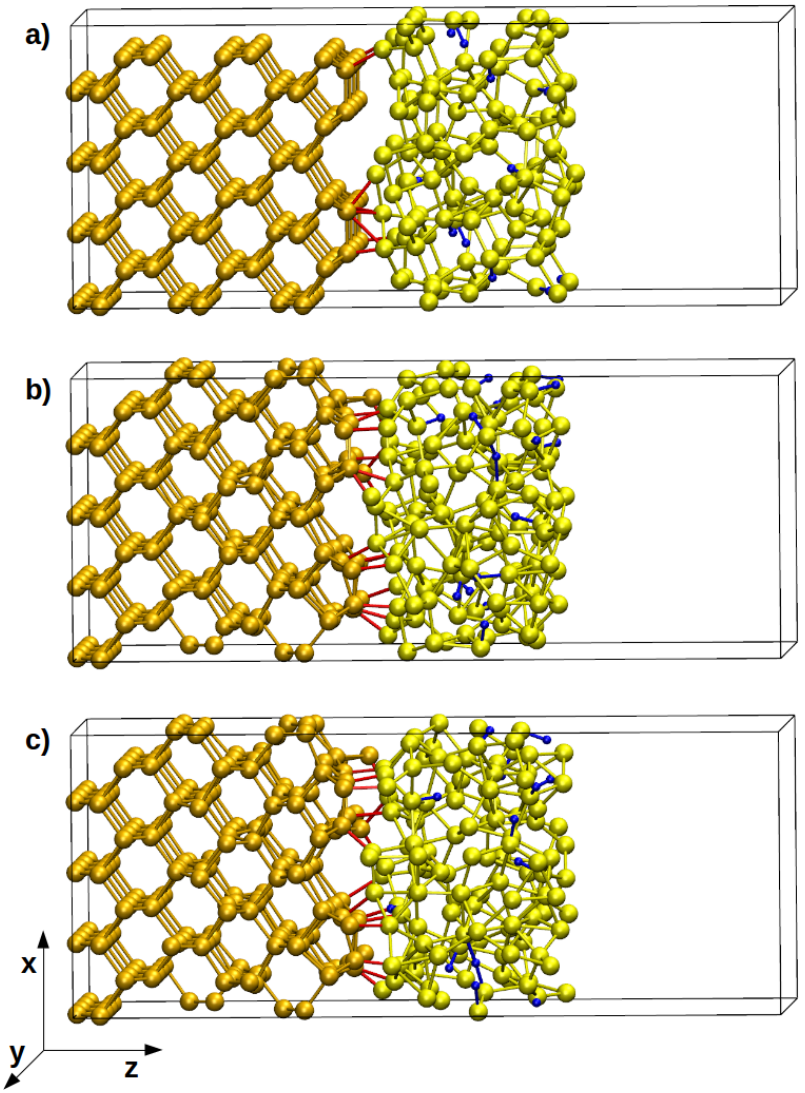

Figure 4: Snapshots of the c-Si/a-Si:H interface in the simulation box. The structure is infinitely extended in both x and y directions. A void region is considered to suppress the interaction, due to periodic boundary conditions, between the external surfaces. Free surfaces and c-Si/a-Si:H interface are perpendicular to y axis. Hydrogen atoms and bonds with Silicon atoms are in blue, Silicon atoms and their bonds are in dark yellow in the c-Si side and are in light yellow in the a-Si:H side. Bonds between c-Si and a-Si are in red. a) initial configuration, b) configuration at 25 ps and c) configuration at 35 ps.

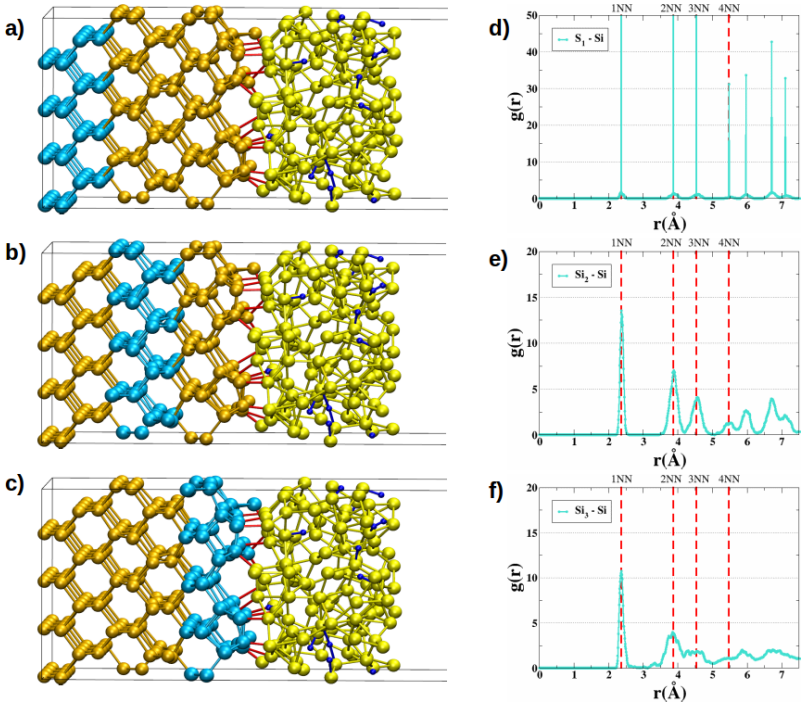

Figure 5: Selected groups of Si atoms S_1, S_2 and S_3 (panels a, b and c) and the corresponding radial pair correlation functions $g(r)$ (panels d, e and f) computed considering the S_i group and the Si atoms. Both S_i and $g(r)$ are depicted in light blue. Red dashed lines indicate the NNs distances of the crystalline phase.

time. At first, total energy calculations of the interface at different distances between c-Si and a-Si:H, were performed to find the interface configuration corresponding to the lowest total energy. The configurations were built moving rigidly by hand the a-Si:H part and keeping fixed the c-Si one. Then, the found configuration is used as starting point for the MD simulation.

2.1 DFT based Molecular Dynamics

The interface shown in Fig. 4a), is used as starting configuration for BOMD simulations on the electronic ground state at constant volume and constant temperature (NVT), with timestep $t_s = 20$ Rydberg atomic units (~ 0.9676 fs) and saving the configurations at every timestep. Ionic temperature is fixed at T = 300 K and is controlled using Andersen thermostat [11]. The first four layers of c-Si atoms on the left are kept fixed to impose a bulk like behaviour to the crystalline silicon part of the system. The MD simulation is performed for more than 35 ps, the first 25 ps of the simulation were used to thermalize the system and reach a stable configuration. The last 10 ps of the simulation (from 25 ps to 35 ps) were used to analyze to system. In panels b) and c) of Fig. 4, are shown the snapshots of the c-Si/a-Si:H interface at 25 ps and 35 ps, respectively.

To characterize the interface we considered distinct groups of Si atoms at different distances from the interface, denominated S_i, with i ranging from 1 to 6. Three sets of atoms: S_1, S_2 and S_3 in the c-Si side (see atoms in light blue in Fig. 5 panels a, b and c), and three sets of atoms: S_4, S_5 and S_6 in the a-Si side (see atoms in light blue in Fig. 6 panels a, b and c). For each group of atoms the radial pair correlation function $g(r)$ is calculated

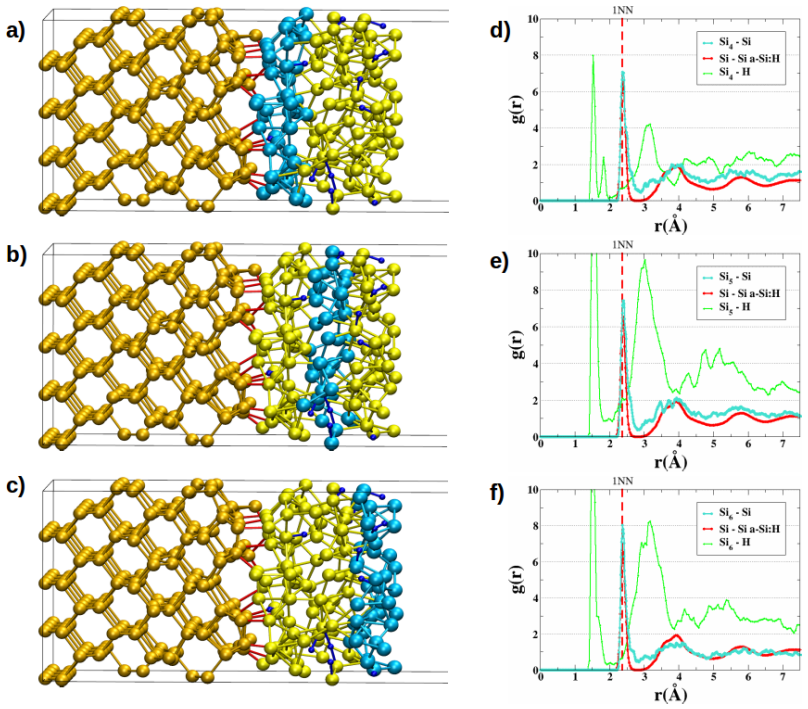

Figure 6: Selected groups of Si atoms S_4, S_5 and S_6 (panels a, b and c) and the corresponding radial pair correlation functions $g(r)$ (panels d, e and f) computed considering the S_i group and the Si atoms (curves in light blue), and considering the S_i group and the H atoms (curves in green). In addition, the $g(r)$ calculated from a-Si:H big system (see Fig. 1 of Ref. [10]) is reported for comparison. Red dashed line indicates the 1NN distance of the crystalline phase.

and averaged in the last 10 ps of simulation, taking one configuration of the system every ten timesteps (one snapshot every 9.676 fs to have more than 1000 configurations overall). In panels d), e) and f) of the Fig. 5 and of the Fig. 6, the light blue curves are the six $g(r)$ computed considering the S_i group and the Si atoms, whereas the green curves are the $g(r)$ computed considering the S_i group (only for i= 4, 5, 6) and the H atoms. Moreover, the $g(r)$ calculated from a-Si:H big system (see Fig. 1 of Ref. [10]) is reported for comparison in the graphs of Fig. 6.

From graph in panel d) of Fig. 5, the $g(r)$ of S_1 has the bulk Silicon behaviour with well-defined peaks corresponding to the NNs (Nearest Neighbors) Si atoms. The second group, S_2, in the middle of the c-Si side, starts to notice the presence of the amorphous Silicon, then the $g(r)$ has less sharped peaks corresponding to the NNs that become broader and loose the shape of the crystalline phase with the increase of the distance r. The presence of the amorphous Silicon is more evident for the c-Si atoms near at the interface (group S_3), as a consequence, $g(r)$ has both the crystalline and amorphous trends. The crystalline shape with well-defined peak corresponding to the 1NN is kept at small distances and is lost increasing r, where the $g(r)$ has a more evident amorphous characteristic.

Graphs in Fig. 6, show S_i-Si radial pair correlation functions (light blue curves) that have trends very similar to that of a-Si:H (red curve), with a peak corresponding to the 1NN Si atoms. Furthermore, the S_i-H $g(r)$ (green curves) point out the Si-H bonds at about 1.5 Å.

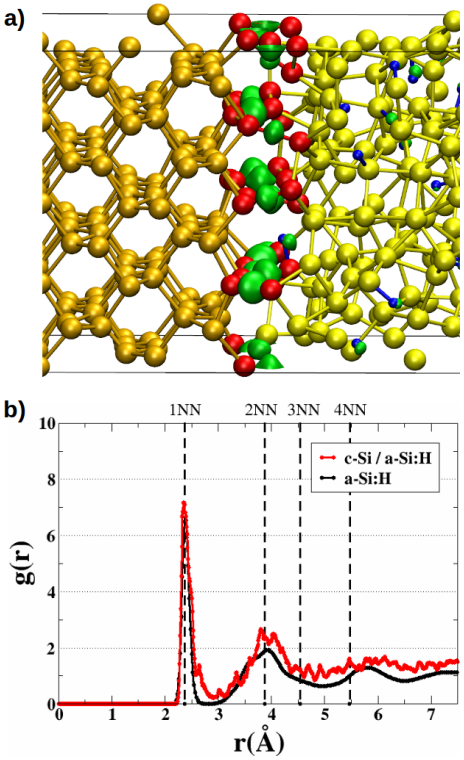

Figure 7: a) S_c, couples of Si atoms formed by one c-Si atom and one a-Si atom at distance lower than 2.9 Å. Green isosurfaces are the electronic density differences between the interface and its components. b) radial pair correlation functions $g(r)$ computed considering the S_c and the Si atoms (red curve). Black dashed lines indicate the NNs distances of the crystalline phase, and the black curve is the $g(r)$ calculated from the a-Si:H big system (see Fig. 1 of Ref. [10]).

In addition, to have a better insight on the interface role, we considered the couples (S_c) of Si atoms formed by one Silicon atom on the c-Si surface and one a-Si atom at distance lower than 2.9 Å. These couples of Si atoms are depicted in red in Fig 7a). As done before we calculated the radial pair correlation functions $g(r)$ taking in consideration S_c and Si atoms (red curve in Fig. 7b). Black dashed lines indicate the NNs distances of the crystalline phase, and the black curve is the $g(r)$ calculated from the a-Si:H big system (see Fig. 1 of Ref. [10]). Obviously, the $g(r)$ have an intermediate trend between the $g(r)$ curves corresponding to the S_3 and S_4 groups. Moreover, we considered the electronic density of the system to point out the formation of bonds at the interface. We subtracted from the electronic density of the interface (ρ_{tot}), the contributions of both the c-Si side (ρ_{c-Si}) and the a-Si:H side ($\rho_{a-Si:H}$), to draw the difference of the electronic densities

$$\rho_{dif} = \rho_{tot} - \rho_{c-Si} - \rho_{a-Si:H}, \tag{1}$$

that is due to the formation of the interface. In Fig. 7a) ρ_{dif} is shown by the green isosurfaces, that are placed between the couples (S_c) of Si atoms and highlights the formation of new bonds.

Finally, a coordination analysis of the couples (S_c) of Si atoms on the interface was done on the last 10 ps of the simulation (see Fig. 8 and Tab. 1). Starting from the S_c atoms on the crystalline side (upper part of Tab.1), we found 1 five-fold coordinated atom (green sphere in Fig. 8a) and 15 atoms with four-fold coordination (red spheres in Fig. 8b). All

these 16 Si atoms are surrounded by others Silicon atoms (gray spheres in panels a) an b) of Fig. 8). With regard to the S_c atoms on the amorphous side (lower part of Tab.1), we found 7 atoms with coordination 5, (green spheres in Fig. 8c). Moreover, we found 9 atoms with coordination 4 (red spheres in Fig. 8d). Finally, 1 atom with coordination 3 is found (light blue sphere in Fig. 8e). Contrary to the others S_c atoms that are surrounded by Si atoms, this atom has two Si atoms and 1 H atom as nearest neighbors (Si2H1). Panel f) summarizes these results, then the S_c atoms are identified on the basis of their coordination; green, red and light blue spheres, for coordination five, four and three, respectively.

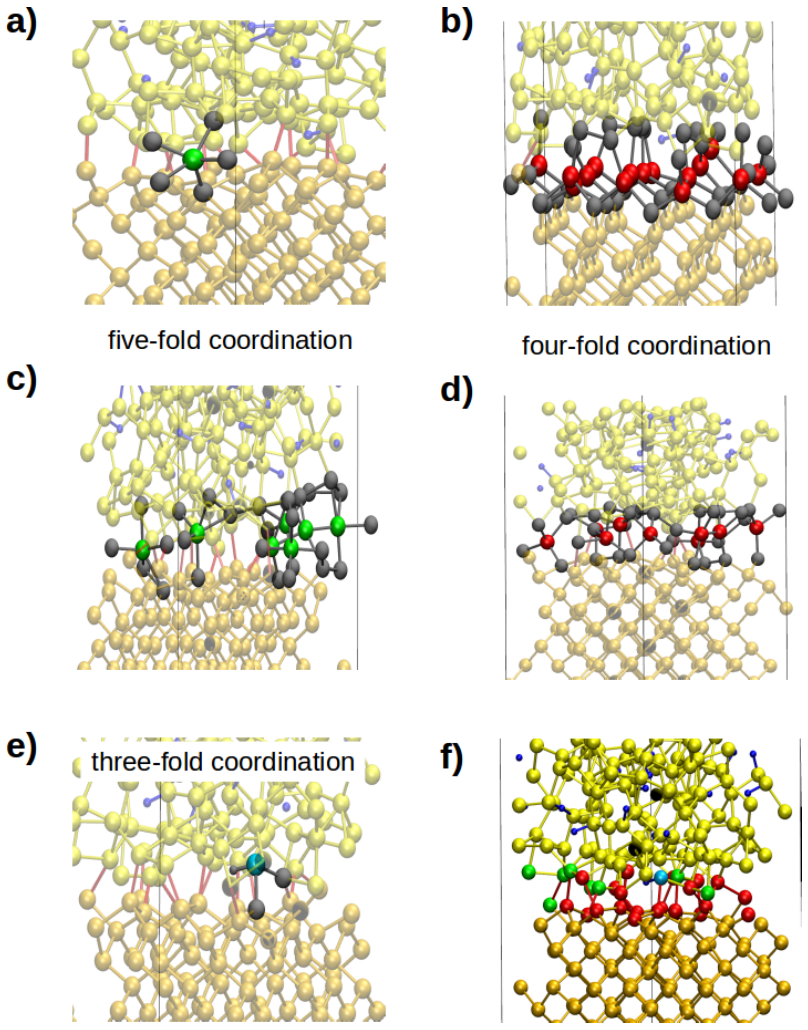

Figure 8: Graphical representation of the coordination analysis of the Silicon atoms on the inteface (S_c). Panels a) five-fold coordinated S_c atom on the c-Si side. Panels b) four-fold coordinated S_c atoms on the c-Si side. Panels c) five-fold coordinated S_c atoms on the a-Si:H side. Panels d) four-fold coordinated S_c atoms on the a-Si:H side. Panels e) three-fold coordinated S_c atoms on the a-Si:H side. in panel f) the S_c atoms are classified on the basis of their coordination. Green, red and light blue sheres, indicate atoms with coordination five, four and three, respectively. Surrounding atoms are depicted by grey spheres.

coord.	index	type index (dist. Å)	
		c-Si	
4	209	Si 193 (2.413) 205 (2.337) 210 (2.440) 226 (2.407)	
	211	Si 195 (2.369) 207 (2.325) 212 (2.329) 316 (2.351)	
	212	Si 196 (2.388) 208 (2.334) 211 (2.329) 227 (2.375)	
	213	Si 193 (2.330) 197 (2.340) 214 (2.485) 313 (2.329)	
	214	Si 194 (2.373) 198 (2.429) 213 (2.485) 248 (2.370)	
	215	Si 195 (2.358) 199 (2.336) 237 (2.418) 350 (2.510)	
	216	Si 196 (2.732) 200 (2.503) 237 (2.554) 313 (2.726)	
	217	Si 197 (2.417) 201 (2.366) 218 (2.489) 348 (2.465)	
	218	Si 198 (2.480) 202 (2.497) 217 (2.489) 273 (2.470)	
	219	Si 199 (2.381) 203 (2.321) 220 (2.396) 231 (2.434)	
	220	Si 200 (2.264) 204 (2.306) 219 (2.396) 349 (2.319)	
	221	Si 201 (2.413) 205 (2.454) 222 (2.460) 228 (2.547)	
	222	Si 202 (2.362) 206 (2.309) 221 (2.460) 239 (2.267)	
	223	Si 203 (2.406) 207 (2.370) 224 (2.387) 351 (2.338)	
	224	Si 204 (2.400) 208 (2.311) 223 (2.387) 229 (2.355)	
5	210	Si 194 (2.450) 206 (2.388) 209 (2.440) 232 (2.391) 249 (2.590)	
		a-Si:H	
3	248	Si 214 (2.370) 350 (2.395)	H 358 (1.510)
4	227	Si 212 (2.375) 287 (2.388) 315 (2.411) 341 (2.338)	
	229	Si 224 (2.355) 230 (2.333) 343 (2.436) 349 (2.278)	
	237	Si 215 (2.418) 216 (2.554) 275 (2.358) 289 (2.555)	
	273	Si 218 (2.470) 238 (2.451) 252 (2.414) 346 (2.761)	
	313	Si 213 (2.329) 216 (2.726) 274 (2.366) 340 (2.355)	
	348	Si 217 (2.465) 228 (2.442) 236 (2.572) 252 (2.356)	
	349	Si 220 (2.319) 229 (2.278) 231 (2.436) 236 (2.387)	
	350	Si 215 (2.510) 232 (2.571) 248 (2.395) 344 (2.439)	
	351	Si 223 (2.338) 239 (2.295) 282 (2.331) 316 (2.410)	
5	226	Si 209 (2.407) 249 (2.616) 258 (2.588) 314 (2.711) 340 (2.469)	
	228	Si 221 (2.547) 238 (2.495) 281 (2.428) 342 (2.730) 348 (2.442)	
	231	Si 219 (2.434) 288 (2.745) 289 (2.338) 338 (2.483) 349 (2.436)	
	232	Si 194 (2.768) 210 (2.391) 316 (2.405) 345 (2.452) 350 (2.571)	
	239	Si 222 (2.267) 233 (2.824) 249 (2.706) 317 (2.453) 351 (2.295)	
	249	Si 210 (2.590) 226 (2.616) 233 (2.427) 239 (2.706) 342 (2.389)	
	316	Si 211 (2.351) 232 (2.405) 277 (2.644) 287 (2.686) 351 (2.410)	

Table 1: Coordination analysis of the Silicon atoms on the inteface (S_c) averaged in tha last 10 ps of simulation run. Data for c-Si(a-Si:H) side of the S_c atoms are reported in the upper(lower) part of the table. In the columns, from left to right, are reported: the coordination number, the index of Si atoms and the details of the surroundings atoms (type, index and distance), respectively.

2.2 CP2K molecular dynamics

In order to have a system with less number of defects on the interface, the last configuration of the c-Si/a-Si:H interface (see Fig. 4c) was used as a starting point for an annealing cycle. Born-Oppenheimer molecular dynamics (BOMD) simulations and electronic structure calculations were performed at the DFT level [12, 13], using the PBE-GGA exchange-correlation functional [14] and periodic boundary conditions (PBC). For the BOMD simulations the Quickstep code of the CP2K suite [15] was used with norm-conserving Goedecker-Tetter-Hutter pseudopotentials [16, 17, 18]. All MD simulations were restricted to the Γ-point. An optimized triple-zeta valence basis set with two polarization orbitals was used. To represent the electron density the gaussians were projected on a real space grid with a planewave cutoff of 280 Ry. The temperature was controlled by a Nosé thermostat [19], and the time step was 1 fs. The temperatures and duration of the annealing steps are reported in Table 2: the sample was heated from 300 K up to 900 K and then cooled very quickly back to 300 K.

Temperature (K)	time (ps)
300	60
500	40
700	40
900	40
700	20
500	21.8
300	21.6

Table 2: Temperatures and duration of the annealing steps.

Fig. 9 shows the number of bonds that have changed during the dynamics with respect to the situation of the configuration at t= 0 ps. The bonds are defined according to a geometrical criteria using a cutoff of 2.70 Å for Si-Si bonds, 1.75 Å for Si-H bonds and 1.0 Å for H-H bonds. There was a very high variation of bonds in the first few ps and during the 500 K and 700 K steps but then the number of changed bonds tended to stabilize.

Fig. 10 reports the number of Si atoms that had fourfold coordination during the dynamics (in the sample there are 320 Si atoms). Analogously Fig. 11 reports the Si atoms with a defective coordination: dangling bonds (coordination = 3) and overcoordinated atoms (coordination = 5). During the dynamics there were sometimes also some very few atoms with coordination 2 and 6.

Fig. 12 shows the variation of the supercell length L_z along the z-axis during the dynamics. This value is calculated considering the center of mass of the surface atoms (the ones with the highest z-value). The increase of L_z is rather higher than what would be expected considering only a thermal expansion effect (although it must be consider that the supercell is constrained to be fixed in the in-plane directions). Instead it correlates well this the decrease of the overcoodinated Si atoms during the 700 K annealing step and the increase of Si atoms with dangling bonds during the 900 K step. Besides it correlates well also with the behavoiur of the z coordinate of the center of mass of H atoms in the amorphous region during the MD reported in Fig. 13. So the L_z increase is a structural effect due to a rearranging of bonds and release of microstresses.

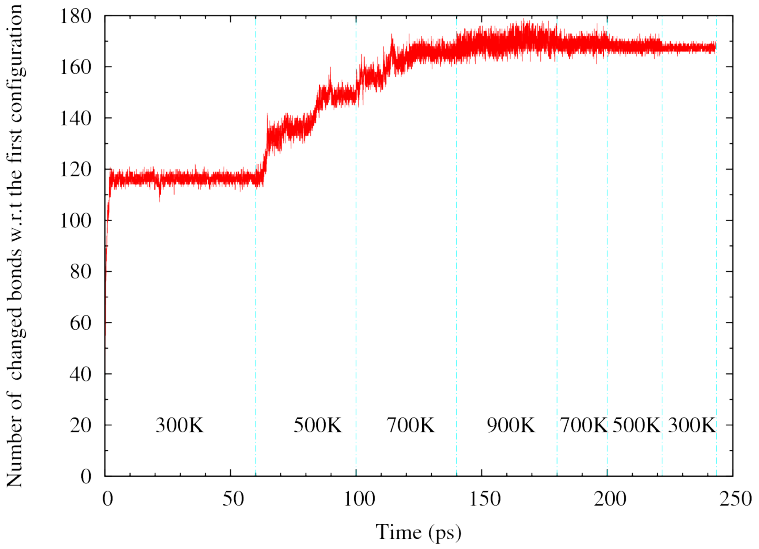

Figure 9: Number of bonds that have changed during the dynamics with respect to the bonds of the configuration at t= 0 ps.

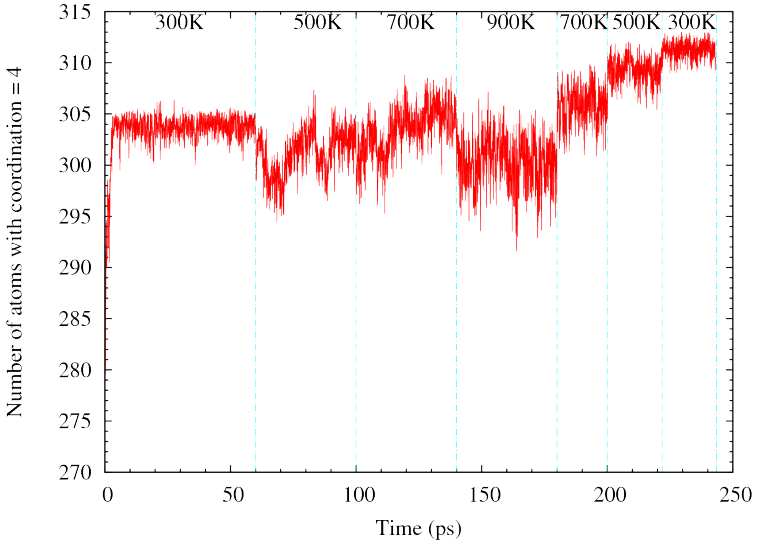

Figure 10: Number of Si atoms with coordination = 4 during the dynamics.

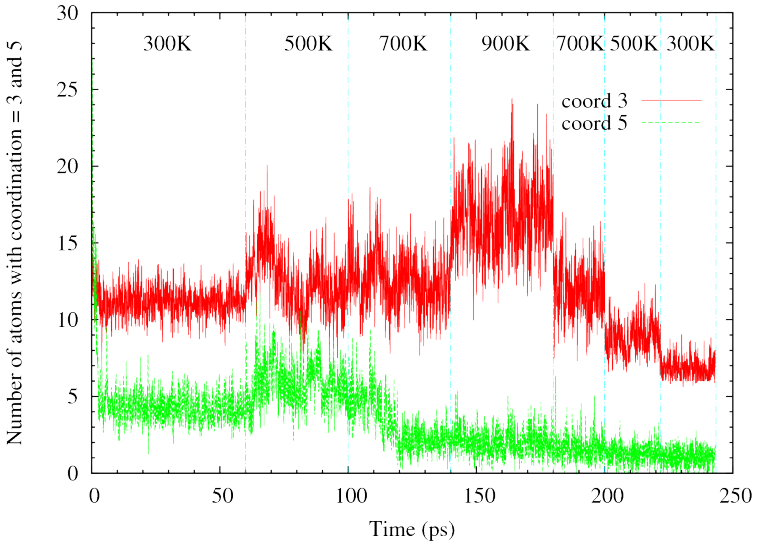

Figure 11: Number of Si atoms with coordination = 3 (red line) and 5 (green line) during the dynamics.

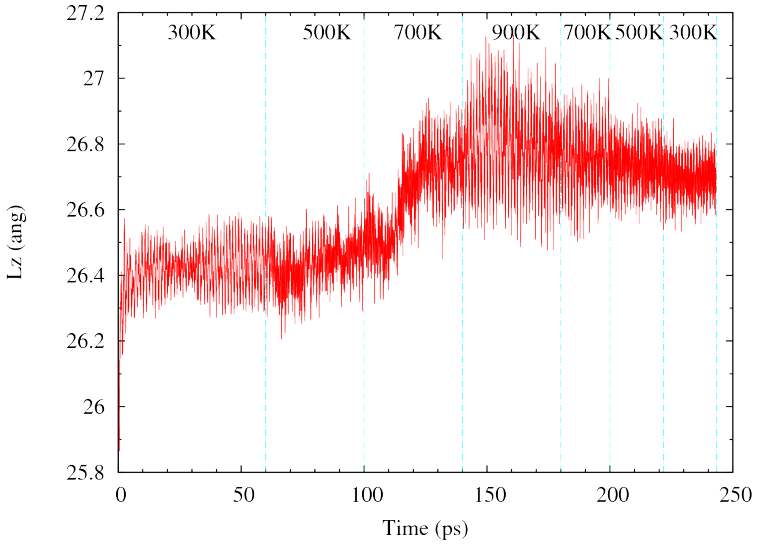

Figure 12: Variation along the z-axis of the length of the supercell during the dynamics.

The final sample obtained at the end of the whole annealing process has a defect free interface with some dangling bonds of the Si atoms in the upper part of the amorphous region (near the surface). No H atoms are present in the interface region.

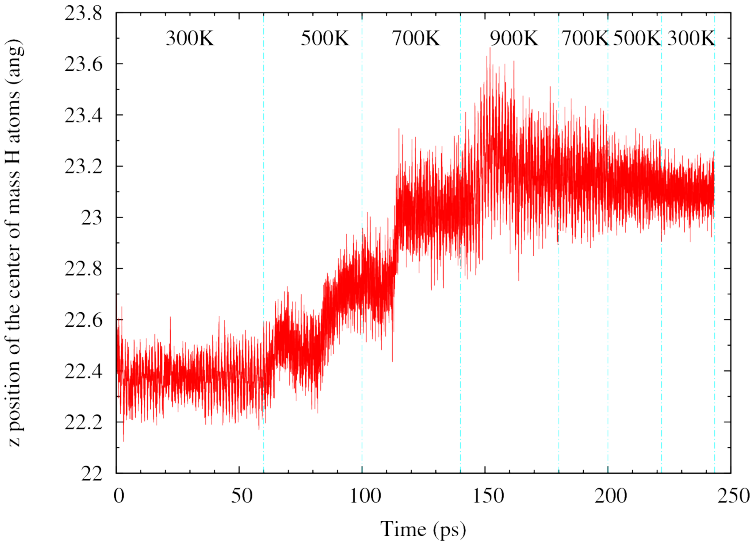

Figure 13: Position of the z coordinate of the center of mass of the H atoms in the amorphous region during the dynamics.

3. Charge transport properties of amorphous crystalline silicon heterointerfaces for solar cells

3.1 *Ab initio* charge carrier transport of across amorphous-crystalline silicon heterointerfaces

In order to link the atomic and electronic structure of the heterointerface as determined from first principles within the EoCoE project to the dynamics of charge carriers, a description of electron transport on ab initio level is investigated. Contrary to the extended plane wave basis used for the electronic structure calculation, ab initio transport is most conveniently dealt with in a localized basis representation. One of the most popular choices for such a basis are the maximally localized Wannier functions (MLWF) [20].

The charge density of states in the Bloch representation is computed using the PWSCF code in the `QuantumESPRESSO` package [21]. A cutoff energy of 450 eV for the wavefunctions is good enough to describe the electronic density of states. The convergence of energy and force are set as 10^{-6} eV and 0.001 eV/$\AA$, respectively. The computed lattice constants are a= b= 5.46 $\AA$ and c= 10.94 $\AA$. The connection between the Bloch and Wannier representation is realized by families of transformations in a continuous space of unitary matrices, which are embedded in the `WanT` code [22]. In the whole process, the choice of a unique set of Wannier functions is the key to construct the accurate Hamiltonian matrix, which is further used for the computation of the transport properties. Meanwhile, the steps of disentanglement and Wannierization are also the most time-consuming procedures.

To rebuild the Bloch wave functions obtained from the density functional theory, there are two widely used sets of initial Wannier functions: one is using a set of atomic

orbitals (e.g., Si p-orbitals), and the other is using a set of one-Gaussian type together with two-Gaussian type orbitals. As a test, a large supercell of 5.46×5.46×10.94 $\AA$ of (bulk) Silicon is used to compute the transport property along the Si[001] direction. For comparison, the average spread Ω in method 2 is 28 Bohr^2, which is about half of that in method 1 (54 Bohr^2). This means that the Wannierization in method 2 is better than in 1.

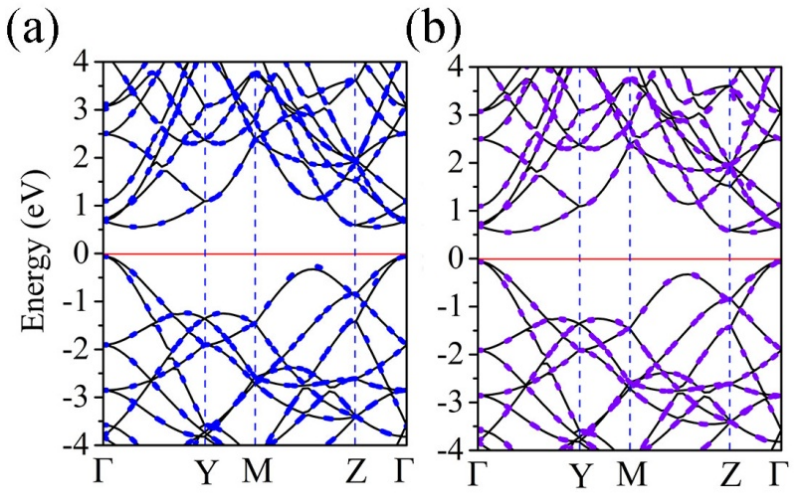

Figure 14: Band structures. The black lines represent the DFT result at the PBE level. (a) The blue dot lines are the Wannier-interpolated bands based on the Si atomic orbitals, and (b) the violet dot lines are the Wannier-interpolated bands based on one- and two- Gaussian type orbitals.

In Fig. 14, the Wannier-interpolated energy bands (dot line) are shown for c-Si both in method 1 and 2, together with the DFT results at the PBE-level (black solid line). Since only the bands around the gap will effectively affect the electronic transport, we mainly focus on the top valence bands and bottom conduction bands around the Fermi level. The chosen set of MLWFs reproduces the band structure of c-Si very well. It has a clear indirect band gap of 0.60 eV in method 1 (0.61 eV in method 2), which is very close to the original DFT results of 0.61 eV. In such a way, the MLWFs method keeps the accuracy of the DFT simulations, but at vastly reduced computational cost.

After the localization of WFs, the Hamiltonian Matrix in the Wannier representation is obtained. Then, the transport is computed based on the Landauer formalism [23]. The transmission function is then expressed in terms of the Green's functions of the conductor and the couplings of the conductor to the leads using the Fisher and Lee formula [24]. Since method 2 is superior to method 1, the quantum conductance is computed using method 2. After obtaining the electronic states, the transport properties of c-Si are then computed using the `WanT` package. The quantum conductance is shown in Fig. 15, where $G_0 = 2e^2/h$ is the quantum unit of conductance, h is Planck's constant and e is the electronic charge.

3.2 NEGF simulation of carrier dynamics at a-Si:H/c-Si interface

For an effective treatment of the interface dynamics using a phenomenological model Hamiltonian, the in-house developed NEGF code `PVnegf`, which is one of the codes that are assessed and optimized towards exascale capability in WP1, is adapted to the simulation of

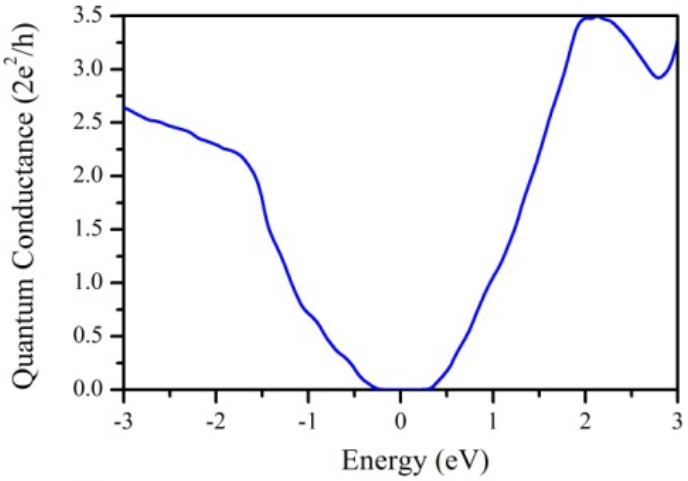

Figure 15: Calculated quantum conductance with the Fermi level set at zero for crystalline silicon along the Si[001] direction.

hole flow across the a-Si:H/c-Si heterointerface. This included in a first stage the complex scattering processes for photogeneration and relaxation of charge carriers in Silicon. For that purpose, a 5-band effective mass Hamiltonian is defined: heavy and light hole bands close to the Γ-point ($\Gamma_{v,h}$, $\Gamma_{v,l}$), longitudinal and transverse X-valley bands with anisotropic effective masses ($X_\parallel$, $X_\perp$), and the conduction band at Γ_c for the virtual intermediate state of the indirect optical transition. The scattering processes that couple these bands and are currently considered in the model include electron-photon scattering between Γ_v and Γ_c for the photogeneration process, $\Gamma_c - X$ electron-phonon scattering for the transfer of photogenerated carriers from the virtual intermediate state to the current-carrying X-valley states, $X - X$ intra- and intervalley electron-phonon scattering (for relaxation of photogenerated carriers in the conduction bands), as well as non-polar-optical electron-phonon scattering in Γ_v bands (for relaxation of photogenerated carriers in the valence bands).

In order to identify the role of multiple bands and electron-phonon interaction on the transfer of photocarrier across the hetero-interface, photocurrent extraction is first simulated in a simplified 3-band model (Γ_v, Γ_c, X) without intraband electron-phonon scattering and applied to an ultra-thin SHJ solar cell. The resulting spectral current flow under monochromatic illumination at photon energy $E_\gamma = 1.2$ eV is displayed in Fig. 16(a). As can be inferred from the ballistic photocurrent and the local density of states in Figs. 16(b) and (c), carrier extraction from the lowest interface states is not possible via direct tunneling, which results in detrimental charge accumulation close to the interface. Figure 17 shows the same situation but for the full 5 band model and with all interactions included. While the LDOS shows a much richer structure and even lower lying interface states, and the tunnel current is enhanced as compared to the ballistic form, also in this case there is no carrier flow directly at the energy of the lowest interface states, which, again, amounts to slow carrier extraction.

3.3 Macroscopic simulation of silicon heterojunction solar cells

Full opto-electronic device simulation on macroscopic continuum level were implemented for the silicon heterojunction solar cells with oxide contact layers as developed

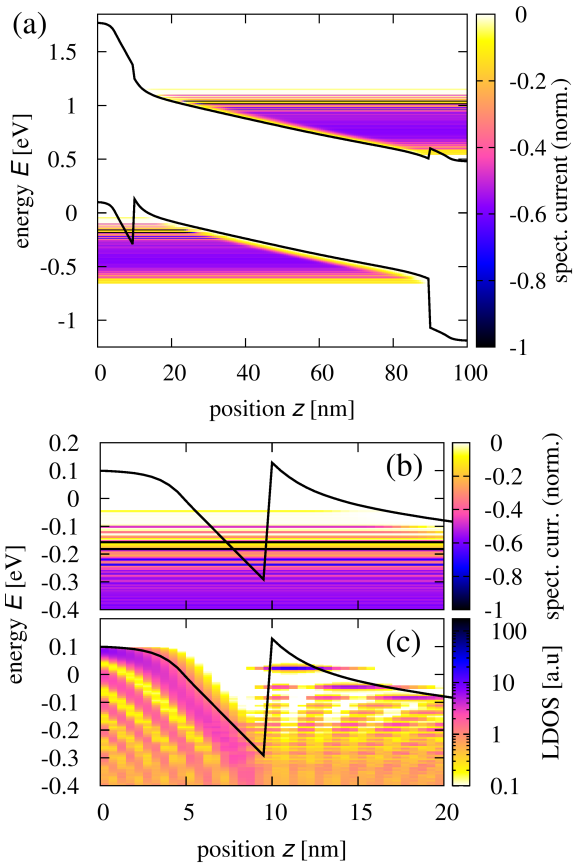

Figure 16: (a) Spectral photocurrent flow in an ultra-thin p-i-n SHJ device under monochromatic illumination (E_γ = 1.2 eV) at a forward bias voltage of V_{bias} = 0.5 V, exhibiting current contributions from tunneling and emission over the barrier. (b) Photocurrent flow across the interface region, revealing the strong impact of (c) the local DOS (1D) with discretization from the doping-induced potential well.[25]

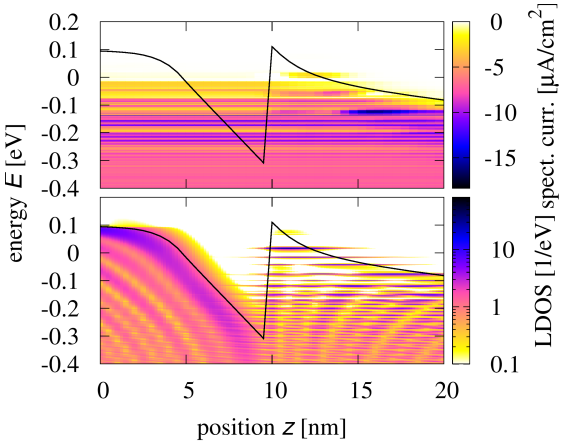

Figure 17: Spectral hole current flow and local density of states at the hetero-interface as obtained from simulations including the presence of multiple bands and intraband carrier-phonon scattering. While phonons enable current flow in a larger spectral range, the lowest interface states are still inaccessible via direct tunneling.

at IEK-5 Photovoltak in Jülich. The coupled Poisson-drift-diffusion equations as well as the optical problem consisting of a combination of the transfer-matrix method with ray-tracing were solved using the integrated TCAD suite `Sentaurus Device` from Synopsys. The structure simulated is shown schematically in Fig. 18(a). As displayed in Fig. 18(b), the experimental current-voltage characteristics are well reproduced by the simulation. While carrier losses at the electrodes and at the interface are considered via surface recombination and recombination at amphoteric defects with Gaussian-like distribution, respectively, tunneling transport is not included yet, which might explain to some extent the lower fill factor as compared to the experiment.

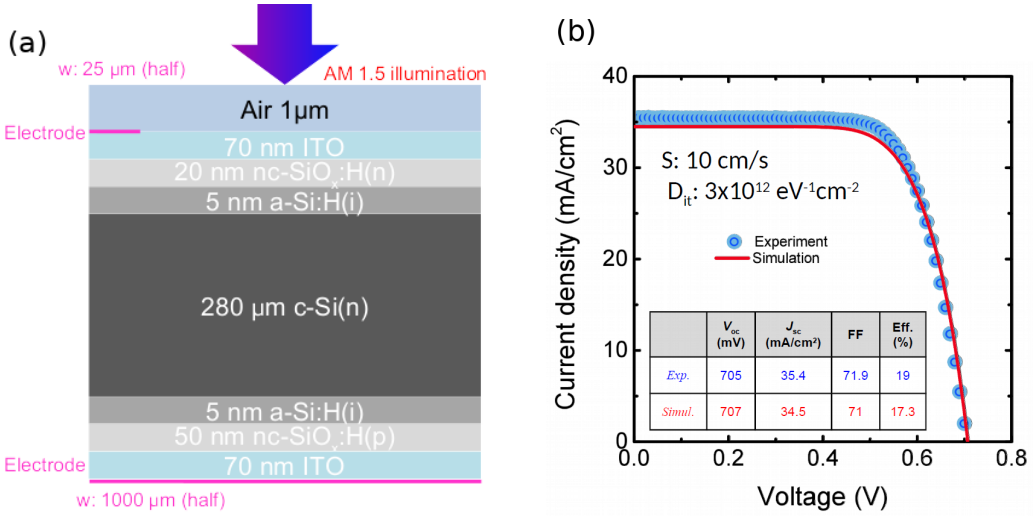

Figure 18: (a) Schematic structure of the Silicon heterojunction solar cells with oxide doping layers as fabricated experimentally and simulated in this work. The electrodes are shown in the actual layout for 2D simulations. (b) Experimental and simulated current-voltage characteristics under AM1.5 spectrum, showing good agreement. The slightly lower fill factor of the simulated curve might be due to the absence of tunneling in the model used.

An important variant of the silicon heterojunction solar cell is the interdigitated back contact (IBC) cell, where the contacts of both polarities are located on the back side of the solar cell. This has the advantage of reduced shading losses and improved surface passivation at the front side. However, the implementation of the concept requires a two-dimensional patterning of the back side, which results in the need for 2D simulations with large local mesh refinement in the lateral dimension, as shown in Fig. 19(a).

A further important element in SHJ solar cell design is the front-side texture for enhanced anti-reflection and light in-coupling. The former effect is induced by optically thin dielectric coating, while the latter requires very large textures in the micron range. A typical texture as used for the simulations is shown in 19(b). Simulation of the combined effect on the light propagation therefore requires a multi-scale simulation approach, which here was chosen to consist of a transfer matrix method (TMM) for the coherent propagation through the thin films and a ray-tracing formalism for the incoherent scattering at the large-scale texture. The approach was tested and verified against the flat cell [Fig. 20(a)], and applied to the textured device, it shows strong photocurrent gain at both short wavelengths (due to enhanced anti-reflection effect) and at long wavelengths (due to enhanced light trapping) as compared to the flat case.

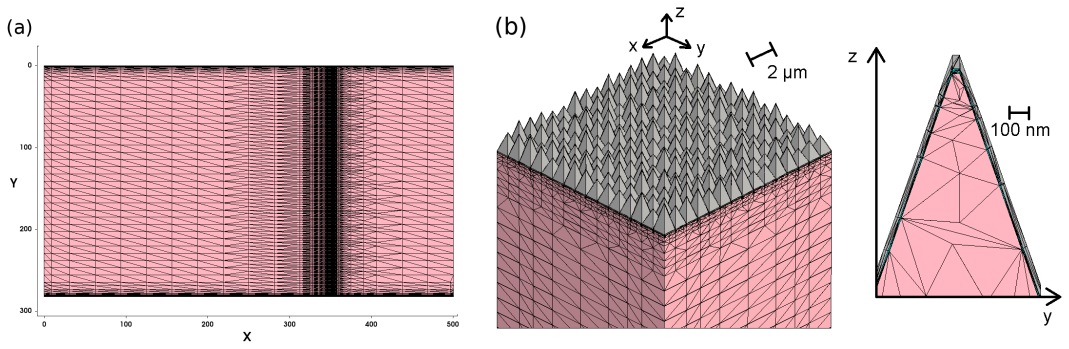

Figure 19: (a) Computational mesh for the 2D electrical simulation of the interdigitated back-contacted solar cell. The region between n- and p-type contact regions needs to be resolved finely in order to obtain an accurate picture of lateral current flow. (b) A typical mesh of a textured front side of a SHJ solar cell. As front side texture, a periodic arrangement of pyramids with a lateral size of 1μm is assumed. The heights of the pyramids are assumed to be randomly distributed. The small figure shows a cut through one particular pyramid to illustrate the refined mesh at the textured interfaces [25].

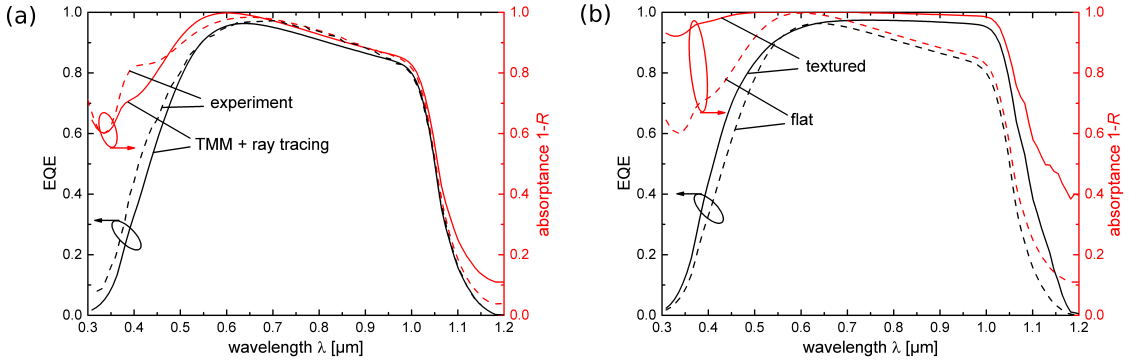

Figure 20: (a) External quantum efficiency and absorptance (1-R) of the flat SHJ solar cell determined from experiment (dashed) and by combining TMM and ray tracing (solid). (b) External quantum efficiency and absorptance (1-R) of the textured SHJ solar cell (solid) and the flat reference cell (dashed) [25].

4. A new method for characterizing supercapacitors: constant applied potential classical density functional theory

In this report we present how two codes, Metalwalls and MDFT have been coupled. Metalwalls is an highly parallel classical molecular dynamics code that allows to simulate solid electrochemical systems, in particular it is possible to imposed a electric potential difference between 2 polarizable electrodes. MDFT is an efficient 3D implementation of molecular density functional theory, an implicit solvent theory that enable to study the thermodynamic solvation properties of any solute in a chemically complex solvent such as water or acetonitrile. Technically, we minimize a functional of the solvent density. This function returns the solvation free energy as its minimum which is attain for the equilibrium solvent density. The objective of this coupling is to drastically reduce the computational cost compared to the full Molecular Dynamic approach, in order to study electrochemical system for energy storage/production. We will first present the adopted scheme to realize this coupling. Some results obtained by this methodology on a simple system composed of two graphene electrode immersed in water are presented and compared to the results obtained with Molecular Dynamics on the same system.

4.1 Technical aspects of the coupling

In this paragraph we will explain the technical details of the coupling between the two codes. In the long term that would be possible to have a self consistent coupling, *i.e.* to write a global functional that will admit as its degrees of freedom the solvent density and the set of charges on the solid atoms. It would then be possible to minimize that functional *i.e.* to simultaneously determine the equilibrium solvent density and the polarization of the metal. This is not the strategy we adopted here: to test the viability of the method we took a more straightforward approach of sequential minimization that is schematize in Fig. 21.

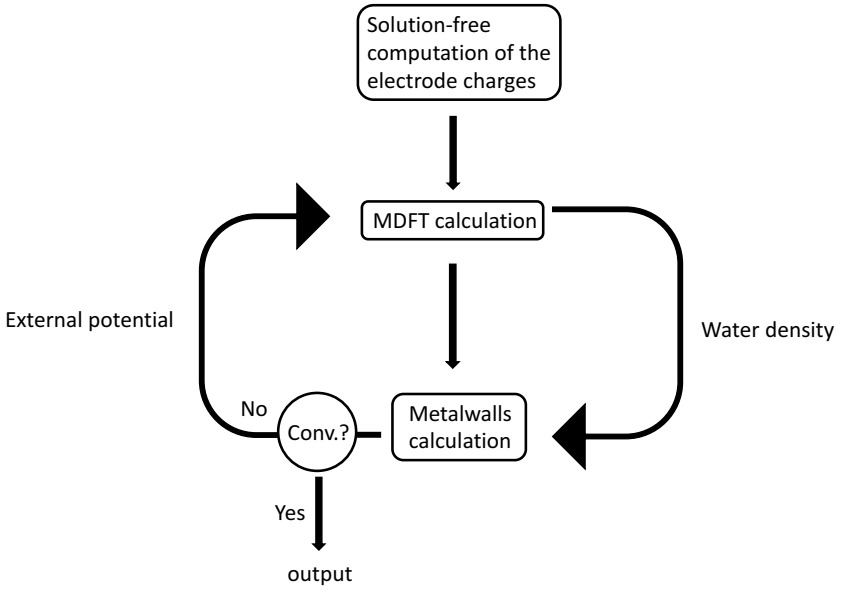

Figure 21: Schematic representation of the coupling.

First we start by a determination of the charges on the solid sites, in absence of the solution using Metalwalls. The electrostatic potential generated by the electrodes is then used as an external potential for the MDFT calculation. After minimization of the functional, the equilibrium water density is obtained. The electrostatic potential generated by this solvent distribution is then used as an external electrostatic potential felt by the electrodes. The polarization of the solid sites, in the presence of that field, is computed using Metalwalls. We iterate this scheme until an convergence criterium is satisfied.

There are two ways to pass the electrostatic field computed with a method to the other one. Either we can directly pass the electrostatic field computed with method A to method B, or we can pass the charges coming from method A to method B, in which the electrostatic potential generated by this charge distribution will be computed. The charges passed to MDFT are the one of the electrode, those passed to Metalwalls are the one of the equilibrium solvent charge density.

We decided to use the solvent charge distribution computed with MDFT in the Metalwalls calculation. The reason for this choice is that in MDFT the electrostatic potential is computed solving the Poisson equation

$$\Delta\Psi(\boldsymbol{r}) = -\frac{n(\boldsymbol{r})}{4\pi\epsilon_0} \tag{2}$$

where n is the orientationally averaged solvent density and ϵ_0 the vacuum permittivity.

This is efficiently done, by taking advantage of Fast Fourier Transform (FFT), in reciprocal space

$$\hat{\Psi}(\boldsymbol{k}) = -\frac{\hat{n}(\boldsymbol{k})}{4\pi \left\|\boldsymbol{k}^2\right\|}, \tag{3}$$

$\boldsymbol{k}$ denoting a wave vector, the hatted quantities denote the Fourier transforms of the non-hatted ones.

However, this implies a 3D Periodic Boundary Conditions (PBC) with the box cell parameters. This is incoherent with Metalwalls in which the system is simulated with a 2D periodicity, there are no periodicity in the direction perpendicular to the electrodes. By passing the solvent charges, the electrostatic potential has the proper 2D periodicity. This potential is then used as the external electrostatic potential in the MDFT calculation, to obtain the equilibrium water density ρ. From this density we then calculate the equilibrium solvent charge density σ according to

$$\sigma(r) = \int \rho(\boldsymbol{r}', \boldsymbol{\Omega}) \sigma_0(\boldsymbol{r} - \boldsymbol{r}', \boldsymbol{\Omega}) d\boldsymbol{r}' d\boldsymbol{\Omega}. \tag{4}$$

This convolution product is handled more efficiently by a multiplication in Fourier space using FFT

$$\hat{\sigma}(\boldsymbol{k}) = \int \hat{\rho}(\boldsymbol{k}, \boldsymbol{\Omega}) \hat{\sigma}_0(\boldsymbol{k}, \boldsymbol{\Omega}) d\boldsymbol{\Omega}. \tag{5}$$

$\boldsymbol{\Omega}$ is an orientation, *i.e.* a compact notation for three Euler angles. $\sigma_0(\boldsymbol{r}, \boldsymbol{\Omega})$ is the charge distribution of a single water molecule located at origin with an orientation $\boldsymbol{\Omega}$ that is expressed as

$$\sigma_0(\boldsymbol{r}, \boldsymbol{\Omega}) = \sum_i q_i \delta(\boldsymbol{r} - \boldsymbol{r}_{i_\Omega}) \tag{6}$$

where δ denotes the Dirac function, the sum run on the solvent sites, q_i is the charge of site i and $\boldsymbol{r}_{i_\Omega}$ is the position of this site when the molecule as an orientation $\boldsymbol{\Omega}$.

Again, there are two ways to pass the effect of the solvent to Metalwalls, either by passing the charge distribution or the electrostatic potential generated by it. For the same reason than before we do not pass the electrostatic potential because it would have been calculated with 3D PBC. Instead we directly pass a set of discrete charges coming from the solvent defined as

$$\{q_i\} = \{\sigma(\boldsymbol{r}_i) \Delta V\} \tag{7}$$

where ΔV is the volume of an elementary voxel of the grid space grid used in MDFT. A standard Metalwalls calculation using this set of charges is restarted and stopped after a single optimization of the charges. The procedure is then iterated until the convergence criterium si reached.

We have not defined a definitive criterium yet but we have several ideas. This criterium can be defined by the relative variation of the charges coming from metalwalls or MDFT, the value of the solvation free energy in MDFT, the variation of the electrostatic potentials coming from the two codes or any combination of those criteria.

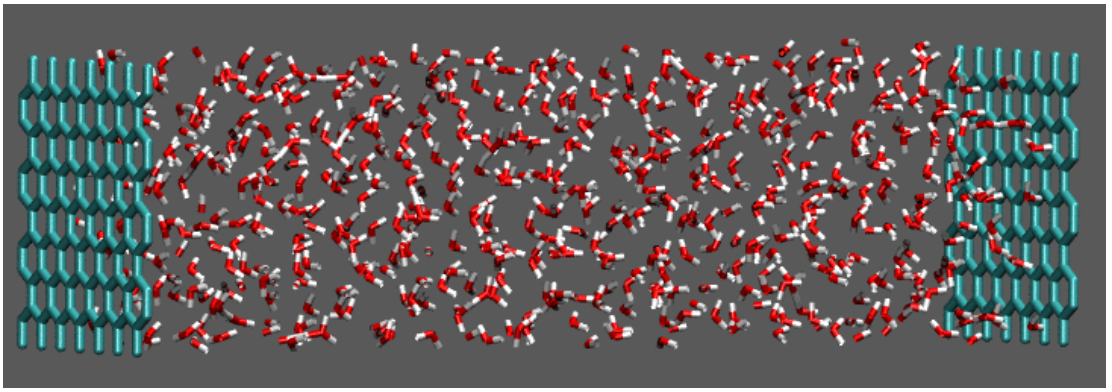

Figure 22: Snapshot of the simulated system in MD. Carbon atoms are in blue, oxygen atoms in red and hydrogen atoms in white.

4.2 Validation and results

Computational details

In this section we report some preliminary results that validate the methodology presented before. The test system on which calculations were run is a simple electrochemical cell composed of two graphene sheets of 17.4 Å by 17.2 Å separated by a distance of 60 Å. Those electrodes are immersed in SPC/E water. The carbon-water interaction is modeled by a Lennard-Jones potential with $\sigma = 3.37$ Å and ϵ= 0.23 kJ/mol for the Carbon atoms and electrostatic interaction. We filled the inter-electrode distance with 540 water molecules to reached a density closed to the bulk one, *i.e.* n_0=0.033 molecules per angstrom cube. A picture of the simulated system is displayed in Fig. 22.

Results

Two MD simulations have been run, in which a potential difference of 1 V and 10 V have been imposed between the two Carbon electrodes for a total duration of 2.1 ns and 5 ns respectively. In Fig. 23 we report the densities of Oxygen and Hydrogen of water molecules along the direction perpendicular to the graphene sheets. Those densities are averaged in planes parallel to the electrode surface. First, we can see that the solvent is structured over a few angstroms and then the bulk value is quickly reached. This value slightly differs within the two simulations techniques, this is because in MD the simulation are run in Canonic ensemble, *i.e.* at fixed number of particle thus the strong absorption at surface cause a slight depletion of molecules in the middle, while in MDFT which is run in the Grand Canonical ensemble the number of particles can vary to counter balance this depletion. Comparing the two methods, the agreement is really good for Oxygen, which is not surprising considering the already reported results. The agreement for the Hydrogen densities, is less satisfying especially for the first layer adsorbed at the left (negative) electrode. This is still not fully understood at this point.

In Fig. 24 we plot the averaged charge density due to the solvent, computed by MD and MDFT. Because this quantity is basically the sum of the O and H densities presented in Fig. 23, it is also not surprising to have a globally good agreement.

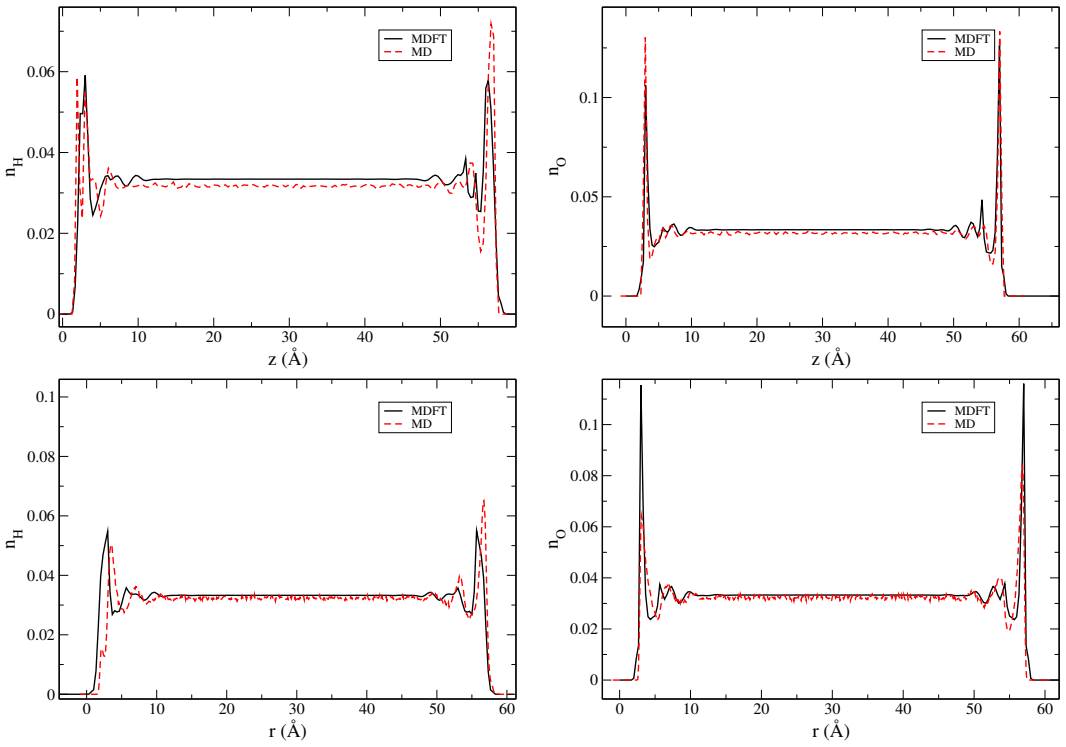

Figure 23: Densities of Oxygen and Hydrogen averaged in planes parallel to the surface of the electrode along the direction perpendicular to the electrode. The results of MD are in dashed red, the ones of MDFT in solid black. The upper figures correspond to a potential difference of 10 V, the lower to a potential difference of 1 V.

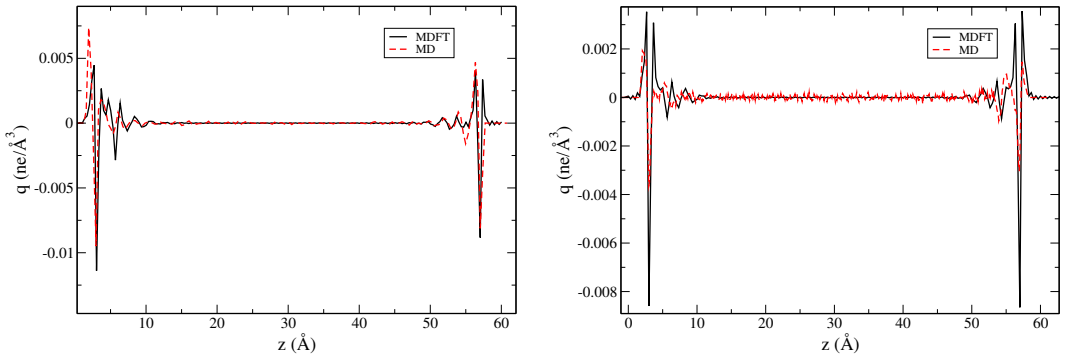

Figure 24: Averaged charge densities of the solvent, in number of elementary charge per angstrom cube along the direction perpendicular to the electrode computed with MD and MDFT with the same color code that in Fig. 23. The left panel correspond to a ΔV of 10 V, the right panel to a ΔV of 1V.

4.3 Conclusions

We have coupled two different codes, Metalwalls that is a 2D MD code that allows to run constant potential simulation and MDFT a molecular density functional theory code. The utilization of an implicit solvent method allows to run constant potential simulation at a much cheaper computational cost that the full MD scheme. First we described the adopted scheme to realize that coupling. We also presented some validation of the methodology by running simulation on a simple system composed of two graphene sheet electrodes immersed in water. The solvent densities and charge densities obtained with this hybrid scheme agree well with the results obtained with a pure MD scheme which make us confident on its use to investigate more complex electrochemical systems. It is now necessary to do not consider only pure solvent but to include electrolyte. We have several strategies to do so, the first would be to include ions at fixed positions, that might be sampled by simple Monte Carlo scheme for instance. Another strategy would be to include the ions at the DFT level, *i.e.* to use a functional that would described a mixture of particles composed of solvent and oppositely charged ions.

References

[1] D. Ghosh, P. Walsh Atkins, M. S. Islam, A. B. Walker, C. Eames. ACS Energy Lett. 2 (2017) 2424.

[2] S. Pering, W. Deng, J. R. Troughton, P. Kubiak, D. Ghosh, R. Niemann, F. Brivio, F. E. Jeffrey, A. B. Walker, M. S. Islam, T. M. Watson, P. Raithby, A. Johnson, S. Lewis, P. J. Cameron. J. Mater. Chem. A 5 (2017) 20658.

[3] R. W. Hockney, J. W. Eastwood. Computer Simulation Using Particles, Taylor and Francis, New York (1988).

[4] C. Lester, R. E. Baker, M. B. Giles, C. A. Yates. Bulletin of Mathematical Biology 78 (2016) 1640.

[5] D. Anderson, D. Higham. SIAM Multiscale Modeling and Simulation 10 (2012) 146.

[6] N. E. Courtier, J. M. Foster, S. E. J. O'Kane, A. B. Walker, G. Richardson. arXiv:1708:09210 (submitted to Phys. Rev. B).

[7] N. E. Courtier, J. M. Cave, J. M. Foster, A. B. Walker, G. Richardson. Submitted to Ener. Env. Sci.

[8] P. Giannozzi, S. Baroni, N. Bonini, M. Calandra, R. Car, C. Cavazzoni, D. Ceresoli, G. L. Chiarotti, M. Cococcioni, I. Dabo, A. Dal Corso, S. de Gironcoli, S. Fabris, G. Fratesi, R. Gebauer, U. Gerstmann, C. Gougoussis, A. Kokalj, M. Lazzeri, L. Martin-Samos, N. Marzari, F.Mauri, R. Mazzarello, S. Paolini, A. Pasquarello, L. Paulatto, C. Sbraccia, S. Scandolo, G. Sclauzero, A. P. Seitsonen, A. Smogunov, Paolo Umari, R. M. Wentzcovitch. J. Phys.: Condens. Matter. 21 (2009) 395502.

[9] www.quantum-espresso.org

[10] EoCoE Deliverable D3.1. ``Porting of codes and atomic scale configurations''.

[11] H. C. Andersen. J. Chem. Phys. 72 (1980) 2384.

[12] P. Hohenberg, W. Kohn. Phys. Rev. 136 (1964) B864.

[13] W. Kohn, L. J. Sham. Phys. Rev. 140 (1965) A1133.

[14] J. P. Perdew, K. Burke, M. Ernzerhof. Phys. Rev. Lett. 77 (1996) 3865.

[15] www.cp2k.org

[16] S. Goedecker, M. Teter, J. Hutter. Phys. Rev. B 54 (1996) 1703.

[17] C. Hartwigsen, S. Goedecker, J. Hutter, Phys. Rev. B 58 (1998) 3641.

[18] M. Krack. Theoretical Chemistry Accounts 114 (2005) 145.

[19] S. Nosé. J. Chem. Phys. 81 (1984) 511.

[20] Nicola Marzari, Arash a. Mostofi, Jonathan R. Yates, Ivo Souza, and David Vanderbilt. Maximally localized Wannier functions: Theory and applications. *Reviews of Modern Physics*, 84(4):1419--1475, October 2012.

[21] P. Giannozzi, S. Baroni, N. Bonini, M. Calandra, R. Car, C. Cavazzoni, D. Ceresoli, G. L. Chiarotti, M. Cococcioni, I. Dabo, A. Dal Corso, S. de Gironcoli, S. Fabris, G. Fratesi, R. Gebauer, U. Gerstmann, C. Gougoussis, A. Kokalj, M. Lazzeri, L. Martin-Samos, N. Marzari, F. Mauri, R. Mazzarello, S. Paolini, A. Pasquarello, L. Paulatto, C. Sbraccia, S. Scandolo, G. Sclauzero, A. P. Seitsonen, A. Smogunov, Paolo Umari and R. M. Wentzcovitch. "Quantum ESPRESSO: a modular and open-source software project for quantum simulations of materials." J. Phys.: Condens. Matter 21 (2009) 395502.

[22] WanT code by A. Ferretti, B. Bonferroni, A. Calzolari, and M. Buongiorno Nardelli (http://www.wannier-transport.org). See also: A. Calzolari, N. Marzari, I. Souza and M. Buongiorno Nardelli. Phys. Rev. B 69 (2004) 035108.

[23] R Landauer. Electrical resistance of disordered one-dimensional lattices. Phil. Mag. 21 (1970) 863.

[24] Daniel S. Fisher and Patrick A. Lee. ``Relation between conductivity and transmission matrix''. Phys. Rev. B 23 (1981) 6851--6854.

[25] U. Aeberhard, P. Czaja, M. Ermes, B. E. Pieters, G. Chistiakova, K. Bittkau, A. Richter, K. Ding, S. Giusepponi, and M. Celino. ``Towards a multi-scale approach to the simulation of silicon hetero-junction solar cells''. J. Green Engineering 5 (2016) 11--32, .